Elastohydrodynamic Scaling Law for Heart Rates

E. Virot,[1,†] V. Spandan,[1,†] L. Niu,[2] W. M. van Rees,[3] and L. Mahadevan[1,2,4,*]
[1]John A. Paulson School of Engineering and Applied Sciences, Harvard University
[2]Department of Physics, Harvard University, Cambridge, Massachusetts 02139, USA
[3]Department of Mechanical Engineering, Massachusetts Institute of Technology, Cambridge, Massachusetts 02138, USA
[4]Department of Organismic and Evolutionary Biology, Harvard University, Cambridge, Massachusetts 02138, USA

(Received 16 December 2019; accepted 4 June 2020; published 28 July 2020)

Animal hearts are soft shells that actively pump blood to oxygenate tissues. Here, we propose an allometric scaling law for the heart rate based on the idea of elastohydrodynamic resonance of a fluid-loaded soft active elastic shell that buckles and contracts axially when twisted periodically. We show that this picture is consistent with numerical simulations of soft cylindrical shells that twist-buckle while pumping a viscous fluid, yielding optimum ejection fractions of 35%–40% when driven resonantly. Our scaling law is consistent with experimental measurements of heart rates over 2 orders of magnitude, and provides a mechanistic basis for how metabolism scales with organism size. In addition to providing a physical rationale for the heart rate and metabolism of an organism, our results suggest a simple design principle for soft fluidic pumps.

DOI: 10.1103/PhysRevLett.125.058102

In living organisms, a characteristic scale determined by the balance between diffusion and uptake rate is typically of the order of 1 mm. On scales larger than this, active devices are necessary to guarantee uniform access to oxygen and efficient elimination of carbon dioxide or excreta. Soft fluidic pumps such as the heart are an evolutionary innovation that solve this problem by enabling internal fluid transport in large multicellular organisms [1,2]. As organism size varies over many orders of magnitude, so does their metabolism [2,3], suggesting a natural question: what are the scaling principles behind the dynamics of the largest and most powerful pump in organisms, the heart [4,5]? A biological argument for the heart rate starts with Kleiber's law [2], i.e., the metabolic rate $\sim$(body mass)$^{3/4}$. Balancing the metabolic rate with the energy consumption rate $\sim$(heart rate) $\times$ (heart blood volume) yields the power law: (heart rate) $\sim$ (body mass)$^{-1/4}$, in reasonable agreement with experimental data [2–4]. However, one may question the fundamental premise of this argument, as the theoretical assumptions underlying Kleiber's law remain under debate [6,7].

Here, we start with a physical argument based on the idea that mechanical resonances in biological systems lead to energy economy [4,8–12]. We will see that this leads to experimentally testable predictions for the heart rate of organisms, from mice to blue whales, that have hearts of different sizes but similar geometries [13], as exemplified in Figs. 1(a) and 1(b). Furthermore, we show that the resulting scaling law provides an alternative basis for Kleiber's law.

The pumping motion of the heart, and particularly that of the left ventricle which pumps oxygenated blood into the body, is driven by the twisting-untwisting dynamics of the cavity which relies on the helical configuration of the ventricular myocardial band [15–17] as shown in Fig. 1(c). Ventricular motion is driven by cardiac muscle cells which contain thick myosin filaments that pull on thin actin filaments during ventricular contraction [18,19]. This results

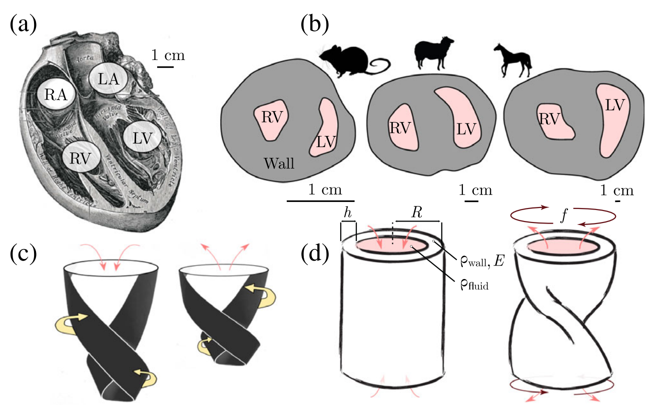

FIG. 1. (a) Structure of a four-chambered heart. LA, LV, RA, and RV denote the left atrium, left ventricle, right atrium, and right ventricle, respectively (drawing adapted from [14]). (b) Transverse section of the ventricles of a rat, sheep, and horse (schematics adapted from [13]). The sections have been enlarged to emphasize their close resemblance. (c) Schematic of the apical loop of the ventricular myocardial band. Adapted from [15]. Periodic twisting and untwisting of the ventricle driven actively by myocardial band contraction leads to fluid pumping. (d) Simplified ventricle geometry, reduced to an elastic shell of thickness h, radius R, density ρ_{wall}, elastic modulus E, and containing a fluid (blood) of density ρ_{blood}. Passive end-twisting of the cylinder causes it to buckle and pump fluid.

in contraction driven stresses within the cardiac muscular tissue that lead it to bend and buckle [20–22], reducing the internal volume of the chamber and forcing the ejection of blood through the aortic valve. Since muscles are only capable of generating contractile stresses, a passive mechanical rebound at the end of ejection would enhance the efficiency of pumping. This is therefore suggestive of an elastohydrodynamic resonance of a fluid-loaded soft elastic shell that is capable of bending and twisting as it ejects fluid over a contraction cycle.

To understand the principle determining the heart rate f_t, we start by assuming that the anatomy of the ventricle can be approximated by that of an elastic shell of radius R and thickness $h < R$, as shown in Fig. 1(d). For relatively thin plates and shells, the bending energy scales as $O(h^3)$ while the stretching energy scales as $O(h)$, so that it is relatively easier to deform a shell by bending it [23]. Thus, it is reasonable to expect that the active stresses induced by muscles will excite the softer bending modes of deformation more easily than the stiffer stretching modes. At a scaling level, the active muscular work required to bend such a shell scales as $Eh^3\kappa^2R^2$, where E is the elastic modulus of the walls and $\kappa \sim A/R^2$ is the wall curvature for a small amplitude of deformation A. This work is converted into kinetic energy of the blood (density ρ_f) that is pushed out of the aorta, and scales as $\rho_f R^3(Af_t)^2$, where we have assumed that the fluid velocity scales as f_tA. Equating the muscular work with the kinetic energy of blood over a cycle yields an estimate for the frequency of a fluid-loaded soft elastic shell as

$$f_t \approx \frac{c_{\mathrm{shape}}}{2\pi}\sqrt{\frac{E}{\rho_{\mathrm{blood}}}\frac{h^{3/2}}{R^{5/2}}}, \tag{1}$$

where c_{shape} is a dimensionless constant that is determined by the shape of the ventricle ($c_{\mathrm{shape}} \simeq 1/2$ for a sphere, and $c_{\mathrm{shape}} \simeq 1/\sqrt{6}$ for a cylinder), first suggested theoretically by one of us in [24]. For a human heart, $h \sim 10$ mm, $R \sim 30$ mm, $E \sim 10^4$ Pa [25,26], and $\rho_f \sim 10^3$ kg/m^3, which gives an elastohydrodynamic resonance frequency $f_t \sim 1$ Hz, in agreement with the observations [27]. For comparison, we also addressed the case of a soft pump dominated by stretching deformations (see Supplemental Material [28]), which leads to different scaling law and a resonance frequency much higher than that measured experimentally.

To further test the idea of the heart as an elastohydrodynamically resonant pump, we now turn to numerical simulations. Our approach builds on and complements the large number of studies on the fluid-structure interaction in coronary flows, heart valve dynamics, and ventricular flows [46–53]. We do this in a simplified setting by starting with an elastic cylindrical shell immersed in a fluid which can deform by bending, shearing, and stretching. For thin and even relatively thick shells, the dominant modes of deformation are those associated with twisting and bending as these are energetically cheaper and thus easier to activate using muscles, consistent with observations of deformation of the heart ventricle [15,54]. Indeed, observations with a rubber cylindrical shell (see Supplemental Material [28] for details and experimental realization for such a model), confirm that twisting leads to a spontaneous buckling instability of the cylinder into a wrinkled tube (with a wavelength that scales with the radius of the cylinder) that also shrinks axially. This mode of deformation reduces the internal volume of the cylinder and thus can be easily harnessed to pump fluid. A full cycle is complete when the cylinder is then brought back to its initial position by untwisting it. The geometry of the shell is characterized by its aspect ratio L/R and thickness ratio R/h, where L, R, and h are the length, radius and thickness of the shell, respectively. In the simulations, we fix the aspect ratio to $L/R = 3$ and vary the thickness ratio h/R, and the shape of the shell is controlled by twisting at one end while keeping the other fixed. A total twist of 90° is imposed at one end and the shape evolution is computed in a quasistatic way by minimizing the bending and stretching energy of the surface [55]. The surface of the cylinder is discretized using approximately 10 000 triangular elements and the material is assumed to be incompressible. The cylindrical shell is immersed in a Cartesian box of size $4L \times 4L \times 4L$ filled with a fluid of kinematic viscosity ν. The boundary conditions imposed on the faces of the Cartesian box perpendicular to the cylindrical axis allow the free flow of fluid into and out of the domain, while free-slip boundary conditions are imposed on the other four faces [37,38]. Through domain dependency tests, we ensure that the boundary conditions and domain size do not influence the final results (see Supplemental Material [28] for details of our numerical model).

In Fig. 2(a), we show snapshots of the shape evolution of the shell from the numerical simulations for a thickness ratio of $R/h = 10$. In Fig. 2(b), we show the net ejection fraction as a function of the driving frequency, in scaled form defined as $\langle \dot{V}_f \rangle / \Delta V_s$ where $\dot{V}_f$ is the net volume of fluid pumped along the axis of the cylinder and ΔV_s is the difference between the initial and final inner volumes of the shell during deformation. The driving Reynolds number, characterizing the ratio of the inertial to viscous forces is defined as $\mathrm{Re} = \pi(2R)^2 f/\nu$, where f is the frequency of the twist-untwist cycle physically imposed on the open face of the cylindrical shell. For each of four different cylinder thickness ratios R/h ($\in [5, 20]$), one can clearly observe a nonmonotonic dependence of the pumping efficiency on the driving Reynolds number. At low Re, due to the dominance of the viscous forces over inertial forces, any fluid pumped out during twisting comes back into the shell during untwisting thus leading

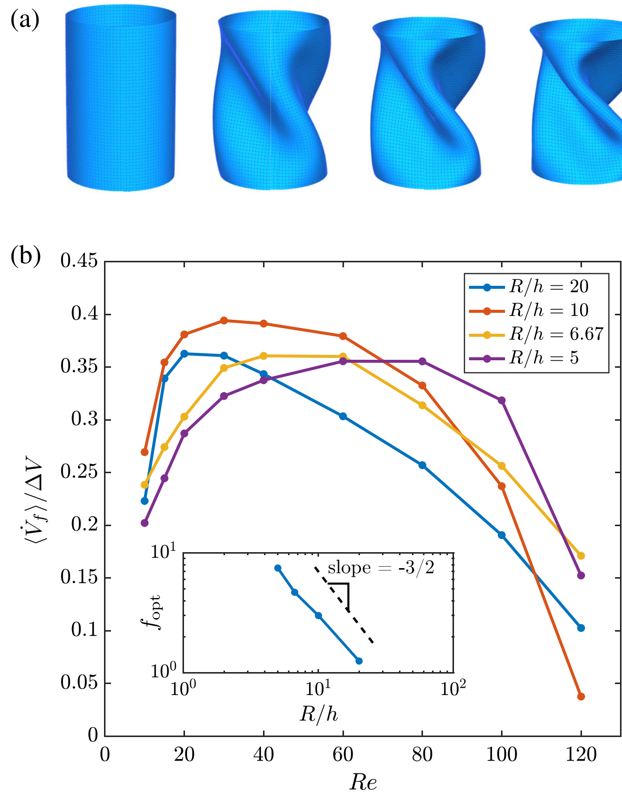

FIG. 2. (a) Snapshots from numerical simulations of a cylindrical shell buckling under twist. The bottom end is kept fixed while the top end is rotated by $\pi/2^c$. The rotation step between each picture is $\pi/6^c$. As the shell buckles into a low-order mode that has an internal volume that is smaller than that of the straight cylinder, it ejects fluid during the process. (b) Net ejection fraction versus the driving Reynolds number for different thickness ratios computed using direct numerical simulations of a deforming elastic shell coupled with a Navier-Stokes solver (see Supplemental Material [28] for details). Inset shows dependence of the frequency with the highest ejection fraction for each thickness ratio versus the thickness ratio which roughly follows a scaling $f \sim (R/h)^{-3/2}$ for fixed $L/R = 3$, consistent with (1).

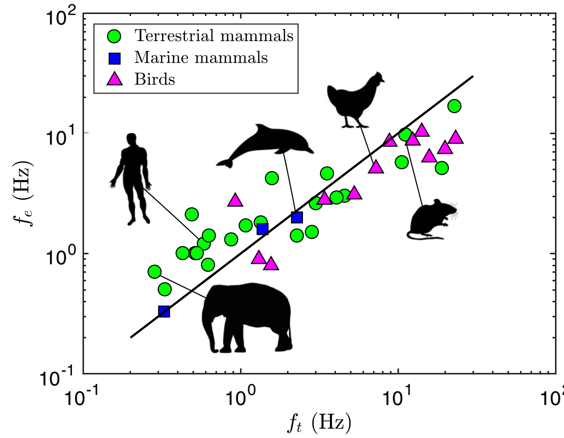

FIG. 3. Comparison between experimentally measured animal heart rates f_e (see Supplemental Material [28]) and the theoretical law for elastohydrodynamic resonance f_t; the straight line is the linear relation (1) $f_e = f_t \simeq c_{\rm shape}/(2\pi)\sqrt{E/\rho_f}h^{3/2}/R^{5/2}$, with $c_{\rm shape} \simeq 1/\sqrt{6}$ (for cylindrical shapes).

to a near-zero net pumping rate. As the driving Re increases, inertial effects come into play which leads to symmetry breaking and net pumping of fluid in one direction along the cylinder axis. When Re is further increased, excessive viscous dissipation from high intensity vorticity regions near the buckles of the cylindrical shell significantly reduces the pumping efficiency. This leads to a nonmonotonicity in the pumping efficiency as a function of Re, and the driving frequency, as seen in Fig. 2(b). Furthermore, despite the relatively small bending strains (which are of the order of $Ah/R^2 \sim 5\%$), we see that a combination of buckling instabilities working in tandem with elastohydrodynamic resonance can lead to ejection fractions of the order of 35%–40%, explaining a long-standing puzzle in heart physiology [54,56].

These numerical simulations confirm that there is an optimal frequency of pumping to maximize ejection fraction in an actively driven elastic cylindrical shell, and that the optimal frequency varies with varying thickness ratio. In the inset of Fig. 2(b), we plot the optimal pumping frequency versus the thickness ratio for the four thickness ratios considered and observe that the frequency roughly follows a scaling $f \sim (h/R)^{3/2}$, consistent with the scaling law (1). The frequency of pumping for a cylindrical shell of a given thickness is optimal when the driving is strong enough to overcome time reversibility in the low Reynolds regime, but not so strong as to produce intense viscous dissipation of the fluid near the buckling regions during the twist-untwist cycle.

To test the theoretical scaling law for the heart rate f_t given by (1), we now compare it with experimental measurements of heart rate f_e across different species [57]. Using data for the average radius and thickness of 38 mammalian and avian left ventricles (see Supplemental Material [28] for details), Fig. 3 shows the experimentally observed heart rate versus the theoretical frequency. We see good agreement between the two in terms of both the trend and, equally importantly, the actual numerical values. Our results are also quantitatively consistent with recent experiments on a tissue-engineered heart ventricle [24] and show that the maximum ejection fraction is achieved when the heart is resonantly forced. Delving deeper into the experimentally observed values of the ventricle radius and its thickness, which together determine the geometrical factor in (1), we find that the typical wall thickness h of the left ventricle is nearly proportional to its typical radius R, with a scaling $h \sim R^\alpha$ where $\alpha = 1.15 \pm .06$ (see Supplemental Material [28] for details). This implies that $f_e \sim f_t \sim R^\beta$, where $\beta = -0.78 \pm 0.09$, in good agreement with experimental data (see Fig. S3 of the Supplemental Material [28]).

We now turn to discuss the implications of our elastohydrodynamic scaling law on metabolic demands in organisms and across species. Since the red blood cell size ($\sim 10\ \mu$m) and the hemoglobin density in the cells (~ 100 g/L) are approximately constant in mammals [2], the volume of oxygen transported within one heartbeat universally scales as the volume of the heart, which itself scales as the volume of the animal [57,58]. The metabolic rate, which is proportional to the rate of oxygen transport, therefore scales as $Q_{\mathrm{metabolic}} \sim R^3 f_t \sim M^\gamma$, where M is the animal body mass and $\gamma = 1 + \beta/3 = 0.74 \pm 0.03$. This combination of structural, dynamic, and functional constraints thus provides an alternative physical basis for Kleiber's law [2], based on the geometry, elasticity, and dynamics of the soft fluid pump that powers organisms. All together, these laws provide a physical basis for the scaling of heart rates and metabolism as a function of body size, consistent with the matching of (heart) form, dynamics, and (physiological and metabolic) function in organisms [61].

Finally our results also suggest a design principle for soft fluidic pumps [24,59,60]: by taking advantage of elastohydrodynamic resonance, they can operate far more efficiently than otherwise. This is consistent with numerical simulations of the coupled elastohydrodynamic problem linking the elastic buckling of thin shells to viscous fluid flow, showing how relatively large ejection fractions can be achieved when the pump is resonantly driven. How this design might have arisen during the evolution of fluidic pumps in natural and engineered systems is a question for the future.

We acknowledge partial support from the NSF-Simons Center for Mathematical and Statistical Analysis of Biology at Harvard DMS-1764269 (L. N., L. M.) and the Harvard Quantitative Biology Initiative (L. N., L. M.), the Swiss National Science Foundation (W. M. v. R.), and NSF DMR-1922321 and DMR-1420570 (L. M.).

[*]Corresponding author.
lmahadev@g.harvard.edu
[†]These authors contributed equally to this work.

[1] S. Vogel, *Vital Circuits: On Pumps, Pipes and the Workings of Circulatory Systems* (Oxford University Press, Oxford, 1993).

[2] K. Schmidt-Nielsen, *Scaling, Why is Animal Size so Important* (Cambridge University Press, Cambridge, 1984).

[3] T. H. Dawson, Allometric relations and scaling laws for the cardiovascular system of mammals, Systems **2**, 168 (2014).

[4] T. A. McMahon and J. T. Bonner, in *On Size and Life* (Scientific American Books, New York, 1983), pp. 111–116.

[5] W. A. Calder, *Size, Function and Life History* (Harvard University Press, Cambridge, 1984).

[6] P. S. Dodds, D. H. Rothman, and J. S. Weitz, Re-examination of the 3/4-law of metabolism, J. Theor. Biol. **209**, 9 (2001).

[7] N. J. B. Isaac and C. Carbone, Why are metabolic scaling exponents so controversial? Quantifying variance and testing hypotheses, Ecol. Lett. **13**, 728 (2010).

[8] M. T. Turvey, R. C. Schmidt, and L. D. Rosenblum, On the time allometry of co-ordinated rhythmic movements, J. Theor. Biol. **130**, 285 (1988).

[9] M. E. DeMont and J. M. Gosline, Mechanics of jet propulsion in the hydromedusan jellyfish, Polyorchis pexicillatus. III A natural resonating bell; the presence and importance of a resonant phenomenon in the locomotor structure, J. Exp. Biol. **134**, 347361 (1988), https://jeb.biologists.org/content/134/1/347.

[10] N. G. Hatsopoulos and W. H. Warren, Resonance tuning in rhythmic arm movements, J. Mot. Behav. **28**, 314 (1996).

[11] E. D. Tytell, C.-Y. Hsu, and L. J. Fauci, The role of mechanical resonance in the neural control of swimming in fishes, Zoology **117**, 48 (2013).

[12] M. Gazzola, M. Argentina, and L. Mahadevan, Gait and speed selection in slender inertial swimmers, Proc. Natl. Acad. Sci. U.S.A. **112**, 3874 (2015).

[13] A. J. Clark, *Comparative Physiology of the Heart* (Macmillan, New York, 1927).

[14] H. Gray, *Anatomy of Human Body* (Lea and Febiger, Philadelphia and New York, 1918).

[15] F. Torrent-Guasp, G. D. Buckberg, C. Clemente, J. L. Cox, H. C. Coghlan, and M. Gharib, The structure and function of the helical heart and its buttress wrapping. I. The normal macroscopic structure of the heart, Semin. Thoracic Cardiovasc. Surg. **13**, 301 (2001).

[16] G. D. Buckberg, Basic science review: The helix and the heart, J. Thoracic Cardiovascul. Surg. **124**, 863 (2002).

[17] S. Nakatani, Left ventricular rotation and twist: Why should we learn?, J. Cardiovasc. Ultrasound **19**, 1 (2011).

[18] T. Burgoyne, F. Muhamad, and P. K. Luther, Visualization of cardiac muscle thin filaments and measurement of their lengths by electron tomography, Cardiovasc. Res. **77**, 707 (2008).

[19] S. G. Page and H. E. Huxley, Filament lengths in striated muscle, J. Cell Biol. **19**, 369 (1963).

[20] F. C. Yin, R. K. Strumpf, P. H. Chew, and S. L. Zeger, Quantification of the mechanical properties of noncontracting canine myocardium under simultaneous biaxial loading, J. Biomech. **20**, 577 (1987).

[21] T. P. Usyk, R. Mazhari, and A. D. McCulloch, Effect of laminar orthotropic myofiber architecture on regional stress and strain in the canine left ventricle, J. Elast. Phys. Sci. Solids **61**, 143 (2000).

[22] F. Viola, V. Meschini, and R. Verzicco, Fluid structure-electrophysiology interaction (FSEI) in the left-heart: A multi-way coupled computational model, Eur. J. Mech. B **79**, 212 (2020).

[23] J. W. S. Rayleigh, *Theory of Sound*, 2nd ed. (Dover, New York, 2013).

[24] L. A. Macqueen, S. P. Sheehy, C. O. Chantre, J. F. Zimmerman, F. S. Pasqualini, X. Liu, J. A. Goss, P. H. Campbell, G. M. Gonzalez, S.-J. Park, A. K. Capulli, J. P. Ferrier, T. F. Kosar, L. Mahadevan, W. T. Pu, and K. K. Parker, A tissue-engineered scale model of the heart ventricle, Nat. Biomed. Eng. **2**, 930 (2018).

[25] T. Romero, J. Covell, and W. F. Friedman, A comparison of pressure-volume relations of the fetal, newborn, and adult heart, Am. J. Physiol. **222**, 1285 (1972).

[26] H. When, E. Bennett, N. Epstein, and J. Plehn, Magnetic resonance imaging assessment of myocardial elastic modulus and viscosity using displacement imaging and phase-contrast velocity mapping, Magn. Reson. Med. **54**, 538 (2005).

[27] R. Rosenthal and R. P. Harvey, *Heart Development and Regeneration* (Academic Press, London, 2010).

[28] See Supplemental Material at http://link.aps.org/supplemental/10.1103/PhysRevLett.125.058102 for details of (i) numerical simulations, (ii) experiments with twist-buckling of a cylindrical shell, (iii) experimental data on heart size and rates across organisms, which includes Refs. [28–44].

[29] C. Weischedel, A. Tuganov, T. Hermansson, J. Linn, and M. Wardetzky, Construction of discrete shell models by geometric finite differences, Fraunhofer ITWM, Kaiserslautern, Germany, Tech. Rep. 220, 2012.

[30] W. M. van Rees, E. Vouga, and L. Mahadevan, Growth patterns for shape-shifting elastic bilayers, Proc. Natl. Acad. Sci. U.S.A. **114**, 11597 (2017).

[31] F. P. Mall, On the muscular architecture of the ventricles of the human heart, Am. J. Anat. **11**, 211 (1911).

[32] R. A. Greenbaum, S. Y. Ho, D. G. Gibson, A. E. Becker, and R. H. Anderson, Left ventricular architecture in man, Br. Hear J. **45**, 248 (1981).

[33] F. Torrent-Guasp, Estructura y funcion del corazon, Revista espanola de cardiologia : publicacion oficial de la Sociedad Espanola de Cardiologia **51**, 91 (1998).

[34] F. Torrent-Guasp, G. D. Buckberg, C. Clemente, J. L. Cox, H. C. Coghlan, and M. Gharib, The structure and function of the helical heart and its buttress wrapping I. The normal macroscopic structure of the heart, Semin. Thoracic Cardiovascul. Surg. **13**, 301 (2001).

[35] M. J. Kocica, A. F. Corno, V. Lackovic, and V. I. Kanjuh, The helical ventricular myocardial band of Torrent-Guasp, Pediatr. Card. Surg. Annu. **10**, 52 (2007).

[36] T. Arts, S. Meerbaum, R. S. Reneman, and E. Corday, Torsion of the left ventricle during the ejection phase in the intact dog, Cardiovasc. Res. **18**, 183 (1984).

[37] V. Spandan, V. Meschini, R. Ostilla-Monico, D. Lohse, G. Querzoli, M. D. de Tullio, and R. Verzicco, A parallel interaction potential approach coupled with the immersed boundary method for fully resolved simulations of deformable interfaces and membranes, J. Comput. Phys. **348**, 567 (2017).

[38] V. Spandan, D. Lohse, M. D. de Tullio, and R. Verzicco, A fast moving least squares approximation with adaptive Lagrangian mesh refinement for large scale immersed boundary simulations, J. Comput. Phys. **375**, 228 (2018).

[39] R. S. Seymour and A. J. Blaylock, The principle of Laplace and scaling of ventricular wall stress and blood pressure in mammals and birds, Physiol. Biomed. Zool. **73**, 389 (2000).

[40] R. Fons, S. Sender, T. Peters, and K. D. Jurgens, Rates of rewarming, heart and respiratory rates and their significance for oxygen transport during arousal from torpor in the smallest mammal, the Etruscan shrew Suncus etruscus, J. Exp. Biol. **200**, 1451 (1997), https://jeb.biologists.org/content/200/10/1451.

[41] C. Weytjens, B. Cosyns, J. D'Hooge, C. Gallez, S. Droogmans, T. Lahoute, P. Franken, and G. Van Camp, Doppler myocardial imaging in adult male rats: Reference values and reproducibility of velocity and deformation parameters, Eur. J. Echocardiogr. **7**, 411 (2006).

[42] G. J. Race, W. L. J. Edwards, E. R. Halden, H. E. Wilson, and F. J. Luibel, A large whale heart, Circulation **19**, 928 (1959).

[43] B. Singh, Morbidity and mortality in cardiovascular disorders: impact of reduced heart rate, J. Cardiovascul. Pharmacol. Therapeuticst **6**, 13 (2001).

[44] E. P. Odum, The heart rate of small birds, Science **101**, 153 (1945).

[45] R. A. Norris, C. E. Connell, and D. W. Johnston, Notes on fall plumages, weights, and fat condition in the ruby-throated hummingbird, Wilson Bull. **69**, 155 (1957), https://www.jstor.org/stable/4158581.

[46] C. S. Peskin, Numerical analysis of blood flow in the heart, J. Comput. Phys. **25**, 220 (1977).

[47] D. McQueen and C. S. Peskin, A three-dimensional computer model of the human heart for studying cardiac fluid dynamics, Comput. Graph. **34**, 56 (2000).

[48] Y. Bazilevs, M.-C. Hsu, D. J. Benson, S. Sankaran, and A. L. Marsden, Computational fluid-structure interaction: Methods and application to a total cavopulmonary connection, Comput. Mech. **45**, 77 (2009).

[49] J. H. Seo, V. Vedula, T. Abraham, and R. Mittal, Multiphysics computational models for cardiac flow and virtual cardiography, Int. J. Numer. Methods Biomed. Eng. **29**, 850 (2013).

[50] A. Updegrove, N. M. Wilson, J. Merkow, H. Lan, A. L. Marsden, and S. C. Shadden, Simvascular: An open source pipeline for cardiovascular simulation, Ann. Biomed. Eng. **45**, 525 (2017).

[51] V. Meschini, M. D. de Tullio, G. Querzoli, and R. Verzicco, Flow structure in healthy and pathological left ventricles with natural and prosthetic mitral valves, J. Fluid Mech. **834**, 271 (2018).

[52] F. Viola, E. Jermyn, J. Warnock, G. Querzoli, and R. Verzicco, Left ventricular hemodynamics with an implanted assist device: An *in vitro* fluid dynamics study, Ann. Biomed. Eng. **47**, 1799 (2019).

[53] Y. Zhang, V. H. Barocas, S. A. Berceli, C. E. Clancy, D. M. Eckmann, M. Garbey, G. S. Kassab, D. R. Lochner, A. D. McCulloch, R. Tran-Son-Tay, and N. A. Trayanova, Multiscale modeling of the cardiovascular system: Disease development, progression, and clinical intervention, Ann. Biomed. Eng. **44**, 2642 (2016).

[54] A. Grosberg and M. Gharib, A dynamical double helical band as a model for cardiac pumping, Bioinspiration Biomimetics **4**, 026003 (2009).

[55] W. M. van Rees, E. A. Matsumoto, A. S. Gladman, J. A. Lewis, and L. Mahadevan, Mechanics of biomimetic 4D printed structures, Soft Matter **14**, 8771 (2018).

[56] A. Grosberg and M. Gharib, Computational models of heart pumping efficiencies based on contraction waves in spiral elastic bands, J. Theor. Biol. **257**, 359 (2009).

[57] W. R. Stahl, Organ weights in primates and other mammals, Science **150**, 1039 (1965).

[58] T. H. Dawson, *Engineering Design of the Cardiovascular System of Mammals* (Prentice Hall, Englewood Cliffs, New Jersey, 1991).

[61] E. R. Weibel, C. R. Taylor, and H. Hoppeler, The concept of symmorphosis: A testable hypothesis of structure-function relationship, Proc. Natl. Acad. Sci. U.S.A. **88**, 10357 (1991).

[59] A. I. Hickerson, D. Rinderknecht, and M. Gharib, Experimental study of the behavior of a valveless impedance pump, Exp. Fluids **38**, 534 (2005).

[60] L. Loumes, I. Avrahami, and M. Gharib, Resonant pumping in a multilayer impedance pump, Phys. Fluids **20**, 023103 (2008).

Supplementary Information for Elastohydrodynamic scaling law for heart rates by

E. Virot, V. Spandan, L. Niu, W. van Rees, and L. Mahadevan

SCALING LAW FOR HEART RATE WHEN DOMINATED BY STRETCHING

To complement the discussion in the main text, here we consider the case of a (thin) shell dominated by stretching deformations. The work required to deform such a shell scales as $E\epsilon^2 R^2 h$, where E is the elastic modulus of the walls and $\epsilon \sim A/R$ is the stretching strain for a small amplitude of deformation A. This work is converted into kinetic energy of the fluid that is pushed out, and scales as $\rho_\mathrm{f} R^3 (A f_\mathrm{t})^2$, where we have assumed that the fluid velocity scales as the product of the frequency f_t and the amplitude A. Balancing the work and kinetic energy yields an estimate for the frequency of such a fluid-loaded & purely stretched soft elastic shell as

$$f_\mathrm{t} \approx \frac{c'_\mathrm{shape}}{2\pi}\sqrt{\frac{E}{\rho_\mathrm{f}}}\ \frac{h^{1/2}}{R^{3/2}}, \tag{S1}$$

where c'_shape is a dimensionless constant that is determined by the shape of the ventricle ($c'_\mathrm{shape} \simeq \sqrt{3}$ for a sphere, and $c'_\mathrm{shape} \simeq \sqrt{2}$ for a cylinder). We note that the scaling law is qualitatively different from the estimate obtained by balancing the bending energy and the kinetic energy (see (1) in the main text) - differing by a factor of h/R. For the dimensions of a human heart, $h \sim 10\,\mathrm{mm}$, $R \sim 30\,\mathrm{mm}$, $E \sim 10^4\,\mathrm{Pa}$ and $\rho_\mathrm{f} \sim 10^3\,\mathrm{kg/m^3}$, which gives an elastohydrodynamic resonance frequency $f_\mathrm{t} \sim 10\,\mathrm{Hz}$, larger than the one obtained when deformations dominated by bending by a factor $\sqrt{12}R/h$. For twist-driven pumping that is the typical mode of ventricular deformation, the shell deforms primarily via twist-induced buckling that leads to bending, so that the scaling law (1) in the main text is the appropriate one to characterize resonant pumping in the heart.

NUMERICAL SIMULATIONS

Elasticity

In order to simulate the twist induced buckling of the cylindrical shell, we minimize the elastic energy for Kirchhoff-Love shells [1]. This energy can be written in terms of the first fundamental form a and second fundamental form b of the mid-surface in the current configuration and the reference configuration (denoted by the subscript 0):

$$\mathcal{E} = \frac{1}{2}\int_U \left[\frac{h}{4}\left\|a_0^{-1}a - I\right\|_e^2 + \frac{h^3}{12}\left\|a_0^{-1}\left(b - b_0\right)\right\|_e^2\right]\sqrt{\det a_0}\ dx\ dy, \tag{S2}$$

The integral is evaluated over the range of parametric coordinates $(x, y) \in U \subset \mathbb{R}^2$, where U defines the parametric domain whose mapping to $\mathbb{R}^3$ corresponds to the mid-surface embedding. The elastic norm $\|\mathbf{A}\|_e^2 = \alpha\mathrm{Tr}^2(\mathbf{A}) + 2\beta\mathrm{Tr}(\mathbf{A}^2)$ defines the invariants of the strain $\mathbf{A}$, with the coefficients $\alpha = E\nu_p/(1-\nu^2)$ and $\beta = E/(2+2\nu_p)$ being the plane-stress Lamé parameters expressed in terms of the Young's modulus E and Poisson's ratio ν_p, of the St. Venant-Kirchhoff material model. We note that, for a thin plate ($b_0 = 0$), when the assumptions of moderate rotations and small in-plane strain assumptions are explicitly taken into account. this energy reduces to the Föppl-van Karman energy [2].

For our discrete approximation of the shell, the first and second fundamental forms of the mid-surface can be written as

$$a_\mathrm{triangle} = \begin{pmatrix} \vec{e}_1 \cdot \vec{e}_1 & \vec{e}_1 \cdot \vec{e}_2 \\ \vec{e}_1 \cdot \vec{e}_2 & \vec{e}_2 \cdot \vec{e}_2 \end{pmatrix}$$

$$b_\mathrm{triangle} = \begin{pmatrix} 2\vec{e}_1 \cdot (\vec{n}_0 - \vec{n}_2) & -2\vec{e}_1 \cdot \vec{n}_0 \\ -2\vec{e}_1 \cdot \vec{n}_0 & 2\vec{e}_2 \cdot (\vec{n}_1 - \vec{n}_0) \end{pmatrix}$$

where $\vec{e}_i$ represent directed edges of the triangle, and $\vec{n}_i$ represent normal vectors defined on all edges of the triangle mesh. The introduction to edge-normal vectors introduces extra degrees of freedom into the mesh; see [1] for an exposition of this choice. This leads to a discretized expression of the elastic energy as a sum over all triangular faces, as further detailed in [1, 2]. The total energy is then minimized with respect to all free mesh vertex positions and the orientation of edge-normal vectors, given the rest configuration and appropriate loading/boundary conditions. The current implementation uses the L-BFGS method to minimize the total energy.

Hydrodynamics

The cylindrical shell is immersed in a fluid, the dynamics of which are computed by solving the incompressible Navier-Stokes equations in a three-dimensional Cartesian domain:

$$\frac{\partial \mathbf{u}}{\partial t} + \mathbf{u} \cdot \nabla \mathbf{u} = -\frac{1}{\rho_{\mathrm{f}}} \nabla p + \nu \nabla^2 \mathbf{u} + \mathbf{f}^{\mathrm{ibm}}, \tag{S3}$$

$$\nabla \cdot \mathbf{u} = 0. \tag{S4}$$

where $\mathbf{u}$ is the fluid velocity vector, ρ_{f} is the density of the fluid and p is the hydrodynamic pressure. $\mathbf{f}^{\mathrm{ibm}}$ is the force needed to enforce the influence of the cylindrical shell on the flow through the immersed boundary method. In the immersed boundary method the boundary condition of any immersed surface (here no-slip) is represented through a momentum source in the governing momentum equations. The equations are solved using an energy-conserving second-order centered finite difference scheme in a Cartesian domain with fractional time-stepping. An explicit Adams-Bashforth scheme is used to discretise the non-linear terms while an implicit Crank-Nicholson scheme is used for the viscous terms. Time integration is performed via a self starting fractional step third-order Runge-Kutta (RK3) scheme. Additional details on the numerical schemes and validation can be found in [9, 10]. The simulations are run in such a way that hydrodynamic stresses do not influence the structural dynamics. This allows us to explicitly test the dependence of pumping dynamics on the twist-untwist frequency.

Dynamics of pumping

In the attached Supplementary movie S1, we show animations of the pumping dynamics when the shell is immersed in the fluid. The dotted lines represent the domain and the flow is visualised in the mid-plane bisecting the cylindrical shell. The colour represents the velocity of the fluid in the axial direction.

EXPERIMENTS ON TWIST BUCKLING OF A CYLINDRICAL SHELL

To realise this experimentally, we build a model of a tubular heart-like pump made of an elastomer that ejects fluid by twisting and bending. The cylindrical shell of constant thickness $h = 2.3$ mm and radius $R = 18.9$ mm is obtained by spincasting a curing solution of silicone at 1000 rpm in a cylindrical mold. The geometry of the shell is characterised by the aspect ratio L/R and thickness ratio R/h, where L, R and h are the length, radius and thickness of the shell, respectively. The shape evolution of such a shell is shown in Fig. S1. Such a device can yield ejection fractions of 50% with bending strains smaller than 30%, as shown in Fig. S2.

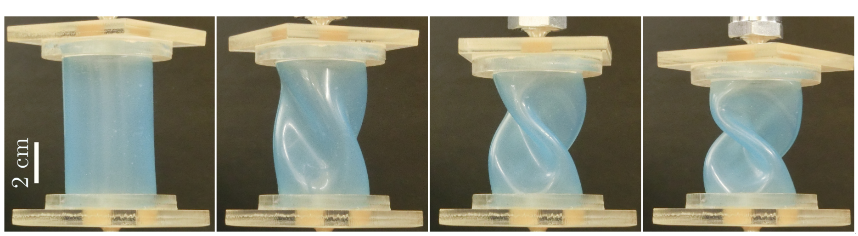

FIG. S1. Artificial pump undergoing controlled instabilities under twist. The shell thickness is $h = 2.3$ mm, its radius is $R = 18.9$ mm, $R/h \simeq 8.2$.

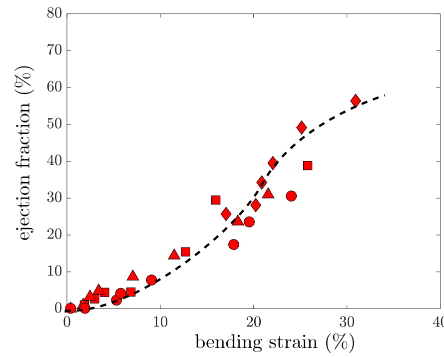

FIG. S2. Ejection fraction as a function of the maximum bending strain of the shell, measured experimentally by determining the radius of curvature of the wrinkles. The different symbols indicate four independent series of tests. The dashed line is a guide for eyes.

HEART SIZE, SHAPE AND RATE DATA

Here we report the references that have been used in Fig. 3 of the main text. R denotes the radius of the left ventricle at the end of the diastole regime. h denotes the average thickness of the left ventricle at the end of the diastole regime. The reported value of the heart rate, f_{e}, is an average on adult male and female specimens. In an individual, the heart rate f_{e} varies as a function of the temperature, stress level, physical activity, disease. Nevertheless, we made the choice to only report the average value for the healthy adult animal. In [11], the wall thickness h is estimated from measurements of the end-diastole volume of the left ventricle and from the myocardial volume.

TABLE S1. Heart geometry and heart rate in terrestrial mammals. (*) The Etruscan shrew heart wall thickness is estimated from the value of R and the best fit $h = 0.21 \times R^{1.15}$ indicated in Fig. S3.

		R (mm)	h (mm)	R/h	f_e (Hz)	sources
Etruscan shrew	*Suncus etruscus*	0.8	0.2*	4.9*	16.7	[12]
Mouse	*Mus musculus*	2.8	0.8	3.5	9.7	[5, 120, 199, 207] in [11]
Rat	*Rattus norvegicus*	3.8	1.9	2.1	5.1	[13]
Rat	*Rattus rattus*	5.1	2.1	2.4	5.7	[56, 87, 88, 106, 113, 127, 134, 136, 177] in [11]
Guinea pig	*Cavia porcellus*	7.2	1.8	4.0	4.6	[7, 81, 83, 87, 107, 132, 167] in [11]
Cat	*Felis domesticus*	11.7	4.8	2.4	3.0	[19, 35, 78, 103, 115, 138] in [11]
Three-toed slot	*Bradypus tridactylus*	11.9	3.1	3.8	1.4	[21, 38, 39, 40, 138] in [11]
Domestic rabbit	*Oryctolagus cuniculus*	12.1	2.5	4.8	4.2	[18, 34, 49, 104, 117, 154, 190] in [11]
Rhesus monkey	*Macaca mulatta*	12.6	4.1	3.1	2.6	[27, 54, 55, 191] in [11]
Cynomolgus monkey	*Macaca fascicularis*	14.3	6.2	2.3	2.9	[27, 30, 100] in [11]
Dog	*Canis familiaris*	27.3	8.7	3.1	1.8	[6, 17, 44, 81, 88, 98, 127, 135, 141, 171, 175, 203, 204] in [11]
Euro kangaroo	*Macropus robustus*	29.4	16.2	1.8	1.5	[121] in [11]
Goat	*Capra hircus*	32.9	8.9	3.7	1.3	[88] in [11]
Human	*Homo sapiens*	33.7	7.1	4.7	1.2	[4, 7, 11, 16, 44, 59, 91, 111, 127, 145, 202] in [11]
Sheep	*Ovis aries*	40.0	8.4	4.8	2.1	[24, 44, 51, 88, 125] in [11]
Pig	*Sus scrofa*	42.1	10.8	3.9	1.4	[88, 169, 200] in [11]
Llama	*Lama glama*	45.9	10.9	4.2	1.0	[4, 41, 60] in [11]
Camel	*Camelus dromedarus*	62.6	18.6	3.4	1.0	[92, 126] in [11]
Cattle	*Bos taurus*	69.1	19.1	3.6	1.0	[88, 95] in [11]
Horse	*Equus caballus*	75.9	28.6	2.7	0.8	[48, 58, 88, 95, 124] in [11]
Giraffe	*Giraffa camelopardalis*	91.0	55.9	1.6	1.7	[193] in [11]
Asian elephant	*Elephas maximus*	134.0	48.4	2.8	0.5	[9, 89] in [11]
African elephant	*Loxodonta africana*	149.5	52.6	2.8	0.7	[89] in [11]

[1] C. Weischedel, A. Tuganov, T. Hermansson, J. Linn, M. Wardetzky Construction of discrete shell models by geometric finite differences (Fraunhofer ITWM, Kaiserslautern, Germany), Technical Report **220** (2012).

[2] W. M. van Rees, E. Vouga, L. Mahadevan Growth patterns for shape-shifting elastic bilayers *Proceedings of the National Academy of Sciences, USA* **114**, 11597-11602 (2017).

[3] F. P. Mall, On the muscular architecture of the ventricles of the human heart, *The American Journal of Anatomy* **2**, 211-266 (1911).

[4] R. A. Greenbaum, S. Y. Ho, D. G. Gibson, A. E. Becker, R. H. Anderson, Left ventricular architecture in man, *British Hear Journal* **45**, 248-263 (1981).

[5] F. Torrent-Guasp, Estructura y funcion del corazon, *Revista Espanola de cardiologia* **51**, 91-102 (1998).

TABLE S2. Heart geometry and heart rate in marine mammals and birds. (*) The hummingbird heart wall thickness and the blue whale left ventricle radius are estimated from the value of R and the best fit $h = 0.21 \times R^{1.15}$ indicated in Fig. S3.

		R (mm)	h (mm)	R/h	f_e (Hz)	sources
Dolphin	*Tursiops truncatus*	37.7	21.1	1.8	2.0	[178] in [11]
Harbor seal	*Phoca virtulina*	38.9	15.9	2.4	1.6	[102] in [11]
Blue whale	*Balaenoptera musculus*	200.0*	94.0	4.4*	0.3	[14, 15]

		R (mm)	h (mm)	R/h	f_e (Hz)	sources
Hummingbird	*Archilochus colubris*	1.5	0.3*	4.4*	10.3	[16, 17]
Canary	*Serinus serinus*	2.8	1.3	2.1	9.0	[137, 207] in [11]
House sparrow	*Passer domesticus*	3.5	1.7	2.0	7.4	[10, 137] in [11]
Starling	*Sturnus vulgaris*	4.6	2.3	2.0	6.3	[207] in [11]
Robin	*Turdus migratorius*	4.8	2.1	2.3	8.7	[207] in [11]
Quail	*Coturnix coturnix*	5.5	2.1	2.6	8.5	[159] in [11]
Pigeon	*Columba livia*	8.2	2.9	2.8	3.1	[10, 71, 82, 161] in [11]
Chicken	*Gallus gallus*	9.4	4.5	2.1	5.1	[142, 186, 187, 197] in [11]
Duck	*Anas platyrhynchos*	13.2	4.8	2.7	2.8	[22, 71, 93, 94, 184] in [11]
Turkey	*Meleagris gallopavo*	15.4	2.6	5.9	2.7	[8, 170] in [11]
Emu	*Dromaius novaehollandiae*	34.3	14.0	2.5	0.8	[70] in [11]
Ostrich	*Struthio camelus*	50.9	24.0	2.1	0.9	[28, 29] in [11]

[6] F. Torrent-Guasp, G. D. Buckberg, C. Clemente, J. L. Cox, H. C. Coghlan, M. Gharib, The structure and function of the helical heart and its buttress wrapping, *Seminars in Thoracic and Cardiovascular Surgery* 13, 301-319 (2001).

[7] M. J. Kocica, A. F. Corno, V. Lackovic, V. I. Kanjuh, The helical ventricular myocardial band of Torrent-Guasp, *Pediatric Cardiac Surgery Annual* , 52-60 (2007).

[8] T. Arts, S. Meerbaum, R.S. Reneman, E. Corday, Torsion of the left ventricle during the ejection phase in the intact dog, *Cardiovascular Research* **18**, 183-193 (1984).

[9] V. Spandan, V. Meschini, R. Ostilla-Monico, D. Lohse, G. Querzoli, M. D. de Tullio, R. Verzicco A parallel interaction potential approach coupled with the immersed boundary method for fully resolved simulations of deformable interfaces and membranes, *Journal of Computational Physics* **348**, 567-590 (2017).

[10] V. Spandan, D. Lohse, M. D. de Tullio R. Verzicco A fast moving least squares approximation with adaptive Lagrangian mesh refinement for large scale immersed boundary simulations, *Journal of Computational Physics* **375**, 228-239 (2018).

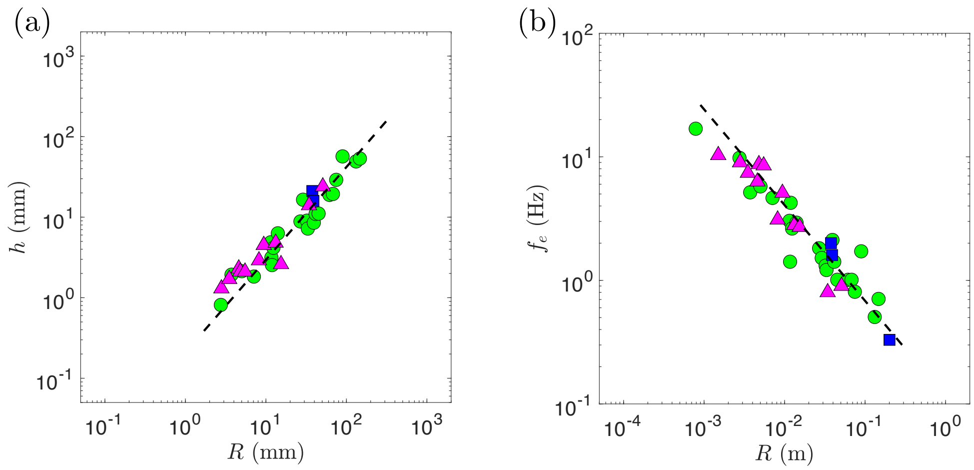

FIG. S3. Left and right panels shows typical wall thickness h of the left ventricle and the experimentally measured heart rate $f_{\rm e}$ as a function of the typical radius R of the left ventricle, respectively. The reported values are the averaged ones (see S.I.). The best fit is given by $h = C_h R^{1.15}$, where h and R are expressed in millimeters (dashed line), and the dimensional constant $C_h = 0.21 mm^{-.15}$. The corresponding prediction in terms of heart rate is given by $f_{\rm e} = f_{\rm t} = C_f R^{-0.78}$, where $f_{\rm e}$ and R are expressed in Hertz and meters respectively (dashed line), and the dimensional constant $C_f = 0.11 Hz.m^{1.78}$. The values of these parameters are averaged over the diastole and the systole. Green circles are terrestrial mammals, blue squares are marine mammals and magenta triangles are birds.

[11] R. S. Seymour, A. J. Blaylock, The principle of Laplace and scaling of ventricular wall stress and blood pressure in mammals and birds, *Physiological and Biomedical Zoology* **73**, 389-405 (2000).

[12] R. Fons, S. Sender, T. Peters, K. D. Jurgens, Rates of rewarming, heart and respiratory rates and their significance for oxygen transport during arousal from torpor in the smallest mammal, the Etruscan shrew *Suncus etruscus*, *Journal of Experimental Biology* **200**, 1451-1458 (1997).

[13] C. Weytjens, B. Cosyns, J. D'Hooge, C. Gallez, S. Droogmans, T. Lahoute, P. Franken, G. Van Camp, Doppler myocardial imaging in adult male rats: Reference values and reproducibility of velocity and deformation parameters, *European Journal of Echocardiography* **7**, 411-417 (2006).

[14] G. J. Race, W. L. J. Edwards, E. R. Halden, H. E. Wilson, F. J. Luibel, A large whale heart, *Circulation* **19**, 928-932 (1959).

[15] B. Singh, Morbidity and mortality in cardiovascular disorders: impact of reduced heart rate, *Journal of Cardiovascular Pharmacology and Therapeuticst* **6**, 13-33 (2001).

[16] E. P. Odum, The heart rate of small birds *Science* **101**, 153-154 (1945).

[17] R.A. Norris, C.E. Connell and D.W. Johnston Notes on fall plumages, weights, and fat condition in the ruby-throated hummingbird, *The Wilson Bulletin* **69**, 155-163 (1957).